

## Moments of the nucleon transverse quark spin densities using lattice QCD

C. Alexandrou,<sup>1,2</sup> S. Bacchio,<sup>2</sup> M. Constantinou,<sup>3</sup> P. Dimopoulos,<sup>4</sup> J. Finkenrath,<sup>2</sup> R. Frezzotti,<sup>5</sup> K. Hadjiyiannakou,<sup>1,2</sup> K. Jansen,<sup>6</sup> B. Kostrzewa,<sup>7</sup> G. Koutsou,<sup>2</sup> G. Spanouides,<sup>2</sup> and C. Urbach<sup>8,9</sup>

<sup>1</sup>*Department of Physics, University of Cyprus, P.O. Box 20537, 1678 Nicosia, Cyprus*

<sup>2</sup>*Computation-based Science and Technology Research Center, The Cyprus Institute, 20 Kavafi Street, Nicosia 2121, Cyprus*

<sup>3</sup>*Department of Physics, Temple University, Philadelphia, Pennsylvania 19122–1801, USA*

<sup>4</sup>*Dipartimento di Scienze Matematiche, Fisiche e Informatiche, Università di Parma and INFN, Gruppo Collegato di Parma Parco Area delle Scienze 7/a (Campus), 43124 Parma, Italy*

<sup>5</sup>*Dipartimento di Fisica and INFN, Università di Roma “Tor Vergata”, Via della Ricerca Scientifica 1, I-00133 Roma, Italy*

<sup>6</sup>*Deutsches Elektronen-Synchrotron DESY, Platanenallee 6, 15738 Zeuthen, Germany*

<sup>7</sup>*High Performance Computing and Analytics Lab, Rheinische Friedrich-Wilhelms-Universität Bonn, Friedrich-Hirzebruch-Allee 8, 53115 Bonn, Germany*

<sup>8</sup>*Bethe Center for Theoretical Physics, Rheinische Friedrich-Wilhelms Universität Bonn, 53115 Bonn, Germany*

<sup>9</sup>*Helmholtz-Institut für Strahlen-und Kernphysik, Rheinische Friedrich-Wilhelms Universität Bonn, 53115 Bonn, Germany*



(Received 2 March 2022; accepted 13 February 2023; published 13 March 2023)

We present the first calculation of the Mellin moments of the transverse quark spin densities in the nucleon using lattice QCD simulations with physical values of the pion mass and in the continuum limit. Specifically, we use three  $N_f = 2 + 1 + 1$  twisted mass fermion gauge ensembles each at different lattice spacings. The densities are extracted from the unpolarized and transversity generalized form factors. The first moment of transversely polarized quarks in an unpolarized nucleon shows an interesting distortion, which can be traced back to the sharp falloff of the transversity generalized form factor  $\bar{B}_{Tn0}(Q^2)$ . The isovector tensor anomalous magnetic moment is determined to be  $\kappa_T = 1.051(94)$ , which confirms a negative and large Boer-Mulders function,  $h_1^\perp$ , in the nucleon.

DOI: [10.1103/PhysRevD.107.054504](https://doi.org/10.1103/PhysRevD.107.054504)

### I. INTRODUCTION

Understanding the spin content of the nucleon from its fundamental constituents, the quarks, and the gluons is a key milestone of nuclear and particle physics. While significant progress has been made in recent years revealing the longitudinal spin structure of the nucleon [1–3], the transverse spin structure remains less known from phenomenology [4–6]. In fact, one of the major goals of the electron-ion collider (EIC) [7], a key experimental facility for nuclear physics being built at Brookhaven, will be to improve the measurements of such quantities. Therefore, an *ab initio* calculation of the transverse spin of the nucleon provides essential information for the EIC physics, as well

as input for other planned experiments, such as the SoLID experiment at Jefferson Laboratory that will measure the transverse momentum structure of the nucleon [8,9]. In addition, evaluating quantities like the tensor charge may reveal physics beyond the Standard Model (SM).

In this paper, we use lattice QCD simulations to study the transverse spin properties of the nucleon. The novelty of this work is composed of the following:

- (i) Avoiding the need of chiral extrapolations that for the nucleon sector can introduce uncontrolled systematic errors by using simulations generated with physical mass values for two mass-degenerate light, strange, and charm quarks, referred to as  $N_f = 2 + 1 + 1$  physical point ensembles;
- (ii) Development of innovative algorithms for the Markov Chain Monte Carlo [10] without which the simulations of such ensembles would not have been possible, as well as for the analysis of the gauge configurations [11]. An example is the multigrid solver adapted for the twisted mass fermion discretization scheme used in this work [12,13] that

---

Published by the American Physical Society under the terms of the [Creative Commons Attribution 4.0 International license](https://creativecommons.org/licenses/by/4.0/). Further distribution of this work must maintain attribution to the author(s) and the published article's title, journal citation, and DOI. Funded by SCOAP<sup>3</sup>.

drastically improves both the simulations and the analysis;

- (iii) The current work is the first to use three physical point ensembles of Wilson-type fermions to take the continuum limit for these quantities;
- (iv) A detailed analysis to eliminate the contribution of excited states to the nucleon matrix elements is performed. This is very important, especially when analyzing physical point ensembles. We use a large number of statistics to keep the statistical errors constant as we search for convergence to the ground state matrix element; and
- (v) Subtraction of lattice artifacts from the required renormalization constants, to all orders in the lattice spacing and to one loop in perturbation theory.

We consider the first two Mellin moments of the three-dimensional (3D) probability densities  $\rho(x, \vec{b}_\perp, \vec{s}_\perp, \vec{S}_\perp)$ , where  $x$  is the longitudinal momentum fraction,  $\vec{s}_\perp$  the transverse quark spin,  $\vec{b}_\perp$  the transverse vector from the center of momentum of the nucleon, and  $\vec{S}_\perp$  the transverse spin of the nucleon. As discussed in Ref. [14], to access the transverse spin densities one needs to compute the twist-two matrix elements of the chiral-even unpolarized and chiral-odd transversity generalized parton distributions (GPDs). The probability density [14] is given as

$$\begin{aligned} \rho(x, \vec{b}_\perp, \vec{s}_\perp, \vec{S}_\perp) &= \frac{1}{2} \left[ H(x, b_\perp^2) + \frac{\vec{b}_\perp^j \epsilon_{ji}}{m_N} (\vec{S}_\perp^i E'(x, b_\perp^2) + \vec{s}_\perp^i \bar{E}'_T(x, b_\perp^2)) \right. \\ &\quad + \vec{s}_\perp^i \vec{S}_\perp^i \left( H_T(x, b_\perp^2) - \frac{\delta_{b_\perp} \tilde{H}_T(x, b_\perp^2)}{4m_N^2} \right) \\ &\quad \left. + \vec{s}_\perp^i (2\vec{b}_\perp^i \vec{b}_\perp^j - \delta^{ij} b_\perp^2) \vec{S}_\perp^j \frac{\tilde{H}_T''(x, b_\perp^2)}{m_N^2} \right], \end{aligned} \quad (1)$$

where  $m_N$  is the nucleon mass,  $\epsilon_{ij}$  is the antisymmetric tensor, and the derivatives are denoted as  $F' \equiv \frac{\partial F}{\partial b_\perp^2}$  and  $\delta_{b_\perp} F \equiv 4 \frac{\partial}{\partial b_\perp^2} (b_\perp^2 \frac{\partial}{\partial b_\perp^2}) F$ . The GPDs,  $H$ ,  $E$ ,  $H_T$ ,  $E_T$ , and  $\tilde{H}_T$  parametrize the generalized quark distributions of twist two and are in general functions of the momentum transfer ( $x$ ), skewness ( $\xi$ ), and squared momentum transfer ( $Q^2$ ) [15]. For the probability density of Eq. (1), the GPDs are needed in impact parameter space at zero skewness ( $\xi = 0$ ) obtained via

$$H(x, b_\perp^2) = \int \frac{d^2 \Delta_\perp^2}{(2\pi)^2} e^{i\vec{b}_\perp \cdot \vec{\Delta}_\perp} H(x, \xi = 0, Q^2), \quad (2)$$

with  $\vec{\Delta}_\perp$  the transverse momentum transfer and  $-Q^2 \equiv \Delta^2$ . Equation (2) for  $H$  generalizes to the other GPDs, and the GPD  $\bar{E}_T$  in Eq. (1) is defined as  $\bar{E}_T = E_T + 2\tilde{H}_T$ .

The moments are then computed as an integral over the momentum fraction as

$$\langle x^{n-1} \rangle_\rho(\vec{b}_\perp, \vec{s}_\perp, \vec{S}_\perp) \equiv \int_{-1}^1 dx x^{n-1} \rho(x, \vec{b}_\perp, \vec{s}_\perp, \vec{S}_\perp), \quad (3)$$

where  $n$  is a positive nonzero integer corresponding to the  $n$ th moment. The GPDs reduce to the generalized form factors (GFFs) if integrated over  $x$ . For the unpolarized case, we have

$$\begin{aligned} A_{n0} &= \int dx x^{n-1} H, \\ B_{n0} &= \int dx x^{n-1} E, \\ \tilde{A}_{n0} &= \int dx x^{n-1} \tilde{H}, \end{aligned} \quad (4)$$

and analogously, for the tensor GFFs,

$$\begin{aligned} A_{Tn0} &= \int dx x^{n-1} H_T, \\ B_{Tn0} &= \int dx x^{n-1} E_T, \\ \tilde{A}_{Tn0} &= \int dx x^{n-1} \tilde{H}_T. \end{aligned} \quad (5)$$

In this work, we are interested in GFFs that parametrize off-forward nucleon matrix elements of local vector and tensor quark operators, defined as

$$\mathcal{O}_V^\mu = \bar{q}(x) \gamma^\mu q(x), \quad \mathcal{O}_V^{\mu\nu} = \bar{q}(x) \gamma^{\{\mu} i \overleftrightarrow{D}^{\nu\}} q(x), \quad (6)$$

$$\mathcal{O}_T^{\mu\nu} = \bar{q}(x) \sigma^{\mu\nu} q(x), \quad \mathcal{O}_T^{\mu\nu\rho} = \bar{q}(x) \sigma^{\{\mu\nu} i \overleftrightarrow{D}^{\rho\}} q(x), \quad (7)$$

where  $\overleftrightarrow{D}$  is the symmetrized covariant derivative,  $\{\dots\}$  denotes symmetrization and subtraction of the trace, and  $[\dots]$  antisymmetrization of the enclosed indices. In what follows, we restrict ourselves to the flavor nonsinglet isovector combination, i.e.,  $\mathcal{O}_V^\mu = \bar{u}(x) \gamma^\mu u(x) - \bar{d}(x) \gamma^\mu d(x)$  for the local vector current and, similarly, for the other three currents defined in Eqs. (6) and (7), where  $u$  and  $d$  are up- and down-quark fermion fields, respectively.

## II. NUCLEON MATRIX ELEMENTS

The relevant quantities entering in the definition of the moments of the transverse densities are the two lowest Mellin moments of the vector and tensor operators given in Eqs. (6) and (7). The nucleon matrix elements of these operators are expanded in terms of GFFs as given below [15] converted to Euclidean space:

- (a) The vector operator  $\mathcal{O}_V^\mu$  that yields the electromagnetic Pauli and Dirac form factors

$$\begin{aligned} \langle N(p', s') | \mathcal{O}_V^\mu | N(p, s) \rangle &= \bar{u}_N(p', s') \left[ \gamma_\mu F_1(Q^2) \right. \\ &\quad \left. - \frac{i\sigma_{\mu\nu} Q^\nu}{2m_N} F_2(Q^2) \right] u_N(p, s), \end{aligned} \quad (8)$$

where in the notation of the previous section,  $A_{10} \equiv F_1$  and  $B_{10} \equiv F_2$ .

- (b) The tensor operator  $\mathcal{O}_T^{\mu\nu}$ , yielding the first Mellin moments of the tensor GFFs

$$\begin{aligned} \langle N(p', s') | \mathcal{O}_T^{\mu\nu} | N(p, s) \rangle &= \bar{u}_N(p', s') \left[ \sigma^{\mu\nu} A_{T10}(Q^2) + i \frac{\gamma^{[\mu} \Delta^{\nu]}}{2m_N} B_{T10}(Q^2) \right. \\ &\quad \left. + \frac{\bar{P}^{[\mu} \Delta^{\nu]}}{m_N^2} \tilde{A}_{T10}(Q^2) \right] u_N(p, s), \end{aligned} \quad (9)$$

with  $\bar{P}^\mu = \frac{p'^\mu + p^\mu}{2}$ . In the forward limit,  $A_{T10}(0)$  gives the tensor charge  $g_T$  which we will denote with  $g_T^{u-d}$  for the isovector case considered here. The combination  $\tilde{B}_{T10}(Q^2) \equiv B_{T10}(Q^2) + 2\tilde{A}_{T10}(Q^2)$  is also quoted instead of  $B_{T10}(Q^2)$ , with  $\tilde{B}_{T10}(0) \equiv \kappa_T$  the anomalous tensor magnetic moment which is related to the Boer-Mulders function  $h^\perp \sim -\kappa_T$ .

- (c) The vector one-derivative operator  $\mathcal{O}_V^{\mu\nu}$ , yielding the second Mellin moments of the unpolarized GFFs

$$\begin{aligned} \langle N(p', s') | \mathcal{O}_V^{\mu\nu} | N(p, s) \rangle &= \bar{u}_N(p', s') \left[ A_{20}(Q^2) \gamma^{\{\mu} \bar{P}^{\nu\}} + B_{20}(Q^2) \frac{i\sigma^{\{\mu\alpha} q_\alpha \bar{P}^{\nu\}}}{2m_N} \right. \\ &\quad \left. + C_{20}(Q^2) \frac{q^{\{\mu} q^{\nu\}}}{m_N} \right] u_N(p, s). \end{aligned} \quad (10)$$

In the forward limit,  $A_{20}(0)$  gives the quark momentum fraction, and specifically  $\langle x \rangle_{u-d}$  in the isovector case. The nucleon spin contributed by the quarks is  $J = \frac{1}{2}[A_{20}(0) + B_{20}(0)]$  in general, and we will use  $J^{u-d}$  to refer to the isovector case, i.e., the isovector quark contribution to the nucleon spin.

- (d) The tensor one-derivative operator  $\mathcal{O}_T^{\mu\nu\rho}$ , yielding the tensor GFFs

$$\begin{aligned} \langle N(p', s') | \mathcal{O}_T^{\mu\nu\rho} | N(p, s) \rangle &= u_N(p', s') \left[ i\sigma^{\mu\nu} \bar{P}^\rho A_{T20}(Q^2) + \frac{\gamma^{[\mu} \Delta^{\nu]}}{2m_N} \bar{P}^\rho B_{T20}(Q^2) \right. \\ &\quad \left. + i \frac{\bar{P}^{[\mu} \Delta^{\nu]}}{m_N^2} \bar{P}^\rho \tilde{A}_{T20}(Q^2) + \frac{\gamma^{[\mu} \bar{P}^{\nu]}}{m_N} \Delta^\rho \tilde{B}_{T21}(Q^2) \right] u_N(p, s), \end{aligned} \quad (11)$$

TABLE I. Parameters for the  $N_f = 2 + 1 + 1$  ensembles used in this work. In the first column we give the name of the ensemble, in the second the lattice volume, in the third  $\beta = 6/g^2$  with  $g$  the bare coupling constant, in the fourth the lattice spacing, and in the fifth the value of  $m_\pi L$ .

Ensemble	$V/a^4$	$\beta$	a [fm]	$m_\pi L$
cB211.072.64	$64^3 \times 128$	1.778	0.07975(32)	3.62
cC211.06.80	$80^3 \times 160$	1.836	0.06860(20)	3.78
cD211.054.96	$96^3 \times 192$	1.900	0.05686(27)	3.90

with the transversity moment given by  $A_{T20}(0)$  that for the isovector case yields  $\langle x \rangle_{\delta u - \delta d}$ . As in the local tensor case, the combination  $\tilde{B}_{T20} \equiv B_{T20} + 2\tilde{A}_{T20}$  may be used instead of  $B_{T20}$ .

The decomposition of the matrix elements for the unpolarized and polarized projectors is given in the Appendix.

### III. LATTICE METHODOLOGY

#### A. Gauge ensembles

We employ the twisted-mass fermion discretization scheme [16,17], which provides automatic  $\mathcal{O}(a)$  improvement [18]. The bare light quark mass is tuned to reproduce the isosymmetric pion mass  $m_\pi = 0.135$  MeV [10,19], while the heavy quark masses are tuned with inputs given by the physical kaon and D-meson masses as well as the D-meson decay constant, following the procedure of Refs. [10,19]. The action also includes a clover term that reduces isospin breaking effects. The parameters of the ensembles analyzed in this work can be found in Table I. The lattice spacing is determined from the nucleon mass, as discussed in Ref. [20].

#### B. Correlation functions

To evaluate the nucleon matrix elements of the operators in Eqs. (6) and (7), we compute three- and two-point correlation functions. The three-point functions are given by

$$\begin{aligned} C^{\mu\nu}(\Gamma; \vec{q}, \vec{p}'; t_s, t_{\text{ins}}, t_0) &= \sum_{\vec{x}_{\text{ins}}, \vec{x}_s} e^{i(\vec{x}_{\text{ins}} - \vec{x}_0) \cdot \vec{q}} e^{-i(\vec{x}_s - \vec{x}_0) \cdot \vec{p}'} \\ &\quad \times \text{Tr}[\Gamma \langle J_N(t_s, \vec{x}_s) \\ &\quad \times \mathcal{O}_{\mathcal{H}}^{\mu\nu}(t_{\text{ins}}, \vec{x}_{\text{ins}}) \bar{J}_N(t_0, \vec{x}_0) \rangle], \end{aligned} \quad (12)$$

where  $q = p' - p$  is the momentum transfer and  $\mathcal{O}_{\mathcal{H}}^{\mu\nu}$  is one of the operators given in Eqs. (6) and (7) with the understanding that for the tensor operator there is an additional index  $\rho$ , while for the electromagnetic current only one index. The initial coordinate  $x_0$  is referred to as the *source* position,  $x_{\text{ins}}$  as the *insertion*, and  $x_s$  as the *sink*.  $\Gamma$  is a projector acting on spin indices, and we will use either the unpolarized  $\Gamma_0 = \frac{1}{2}(1 + \gamma_0)$  or the three polarized

TABLE II. The number of Gaussian smearing iterations  $n_G$  and the Gaussian smearing parameter  $\alpha_G$  used for each ensemble. We also provide the number of APE-smearing iterations  $n_{\text{APE}}$  and parameter  $\alpha_{\text{APE}}$  applied to the links that enter the Gaussian smearing hopping matrix. The resulting source rms radius obtained is given in the last column where the error is due to the uncertainty in the lattice spacing.

Ensemble	$n_G$	$\alpha_G$	$n_{\text{APE}}$	$\alpha_{\text{APE}}$	$\sqrt{\langle r^2 \rangle_\psi}$ [fm]
cB211.072.64	125	0.2	50	0.5	0.461(2)
cC211.060.80	140	1.0	60	0.5	0.516(2)
cD211.054.96	200	1.0	60	0.5	0.502(3)

$\Gamma_k = \Gamma_0 i\gamma_5 \gamma_k$  combinations and  $J_N$  the standard nucleon interpolating operator  $J_N(x) = \epsilon_{abc} u^a(x) [u^{b\dagger}(x) \mathcal{C} \gamma_5 d^c(x)]$ , where  $u$  and  $d$  are up- and down-quark spinors and  $\mathcal{C} = \gamma_0 \gamma_2$  is the charge conjugation matrix.

To increase the overlap of the interpolating operator  $J_N$  with the proton state and decrease overlap with excited states, we use Gaussian smeared quark fields [21,22] given by

$$\psi_{\text{smear}}^a(t, \vec{x}) = \sum_{\vec{y}} F^{ab}(\vec{x}, \vec{y}; U(t)) \psi^b(t, \vec{y}), \quad (13)$$

where  $F = (\mathbf{1} + \alpha_G H)^{n_G}$  and  $H(\vec{x}, \vec{y}; U(t)) = \sum_{i=1}^3 [U_i(x) \delta_{x,y-i} + U_i^\dagger(x - \hat{i}) \delta_{x,y+i}]$  with APE smearing [23] applied to the gauge fields  $U_\mu$  entering the Gaussian smearing hopping matrix  $H$ . The parameters used for Gaussian and APE smearing for each ensemble are given in Table II, tuned separately for each ensemble. Namely, we tune the source root-mean-squared (rms) radius, defined as  $\langle r^2 \rangle_\psi = \frac{\sum_{\vec{r}} \vec{r}^2 \psi_{\text{smear}}^\dagger(\vec{r}, t) \psi_{\text{smear}}(\vec{r}, t)}{\sum_{\vec{r}} \psi_{\text{smear}}^\dagger(\vec{r}, t) \psi_{\text{smear}}(\vec{r}, t)}$  to be  $\sim (0.5 \text{ fm})^2$ , with the precise values obtained listed in Table II.

The connected three-point functions are computed using sequential propagators inverted through the sink, i.e., using the so-called *fixed-sink* method. This requires new sequential inversions for each sink momentum, and we therefore restrict to  $\vec{p}' = 0$ , meaning the source momentum  $\vec{p}$  is determined via momentum conservation by the momentum transfer as  $\vec{p} = -\vec{q}$ . For the twisted-mass formulation employed here, the disconnected quark loop contributions are order  $a^2$  for finite  $a$  and vanish in the continuum limit [16].

### C. Analysis of excited states

Connected three-point functions are computed using several time separations,  $t_s$ , between the application of the creation and annihilation nucleon interpolating operators, namely  $t_s \in [0.64, 1.6]$  fm for the cB211.072.64,  $t_s \in [0.55, 1.51]$  fm for the cC211.06.80, and  $t_s \in [0.46, 1.14]$  fm for the cD211.054.96 ensemble, as shown

in Table III. This broad range of separations is necessary for a thorough investigation and elimination of excited state contributions. At constant statistics, the noise-to-signal ratio increases exponentially with  $t_s$  and the increase is exacerbated at the physical point. We, thus, increase the number of measurements with increasing  $t_s$  in physical units by increasing the number of source positions ( $n_{\text{src}}$ ), as shown

TABLE III. Statistics for computing the isovector matrix elements for the cB211.072.64 (left table), the cC211.060.80 (middle table), and the cD211.054.96 (right table) ensemble. In each table, we provide the sink-source separations used in lattice (first column) and physical (second column) units and the number of source positions per configuration (third column). For each ensemble, the bottom row indicates the number of source positions used for the two-point functions.

cB211.072.64		
750 configurations		
$t_s/a$	$t_s$ [fm]	$n_{\text{src}}$
8	0.64	1
10	0.80	2
12	0.96	4
14	1.12	6
16	1.28	16
18	1.44	48
20	1.60	64
Nucleon 2pt		264
cC211.060.80		
400 configurations		
$t_s/a$	$t_s$ [fm]	$n_{\text{src}}$
6	0.41	1
8	0.55	2
10	0.69	4
12	0.82	10
14	0.96	22
16	1.10	48
18	1.24	45
20	1.37	116
22	1.51	246
Nucleon 2pt		650
cD211.054.96		
500 configurations		
$t_s/a$	$t_s$ [fm]	$n_{\text{src}}$
8	0.46	1
10	0.57	2
12	0.68	4
14	0.80	8
16	0.91	16
18	1.03	32
20	1.14	64
Nucleon 2pt		368

in Table III, to keep an approximately constant error for all  $t_s$ . Also we point out that for a given  $t_s$  we increase statistics as we decrease  $a$ . Indicatively, for  $t_s = 0.96$  fm we use a total of  $750 \times 4 = 3,000$  and  $400 \times 22 = 8,800$  measurements for the cB211.072.64 and cC211.060.80 ensembles, respectively, and for  $t_s = 1.03$  fm  $500 \times 32 = 16,000$  measurements for the cD211.054.96 ensemble. As regards autocorrelations, in our setup and for the quantities considered, we observe no increase in autocorrelation for the involved correlators when going from the coarsest to the finest ensemble.

To obtain the desired ground state matrix element, we take an appropriate ratio of three- to two-point functions as done in our previous studies, e.g., in Refs. [24–26],

$$\begin{aligned} R^{\mu\nu}(\Gamma; \vec{p}; t_s, t_{\text{ins}}) &= \frac{C^{\mu\nu}(\Gamma; \vec{p}; t_s, t_{\text{ins}})}{C(\Gamma_0; t_s)} \\ &\times \sqrt{\frac{C(\Gamma_0, \vec{p}; t_s - t_{\text{ins}})C(\Gamma_0, 0; t_{\text{ins}})C(\Gamma_0, 0; t_s)}{C(\Gamma_0, 0; t_s - t_{\text{ins}})C(\Gamma_0, \vec{p}; t_{\text{ins}})C(\Gamma_0, \vec{p}; t_s)}}, \end{aligned} \quad (14)$$

where from now on  $t_s$  and  $t_{\text{ins}}$  are taken to be relative to the source  $t_0$ , i.e., we assume  $t_0 = 0$  without loss of generality, and we drop the sink momentum ( $\vec{p}'$ ) as an argument to the three-point function since as mentioned in our setup we use  $\vec{p}' = 0$  throughout. The two-point functions appearing in the ratio are given by

$$\begin{aligned} C(\Gamma_0, \vec{p}; t_s, t_0) &= \sum_{\vec{x}_s} e^{-i(\vec{x}_s, -\vec{x}_0) \cdot \vec{p}} \\ &\times \text{Tr}[\Gamma_0 \langle J_N(t_s, \vec{x}_s) \bar{J}_N(t_0, \vec{x}_0) \rangle]. \end{aligned} \quad (15)$$

In the limit of large time separations,  $(t_s - t_{\text{ins}}) \gg a$  and  $t_{\text{ins}} \gg a$ , the lowest state dominates, and the ratio becomes time independent:

$$R^{\mu\nu}(\Gamma; \vec{p}; t_s, t_{\text{ins}}) \xrightarrow[t_{\text{ins}} \gg a]{t_s - t_{\text{ins}} \gg a} \Pi^{\mu\nu}(\Gamma; \vec{p}). \quad (16)$$

An essential step in any analysis of lattice QCD matrix elements is to ensure that contributions from excited states to the ground state matrix elements are sufficiently suppressed. To this end we compare results from the following three methods.

### 1. Plateau method

In this method we use the ratio in Eq. (14) in search of a time-independent window (plateau) and extract a value by fitting to a constant. We then seek convergence of the extracted plateau value as we increase  $t_s$  that then produces the desired matrix element.

### 2. Two-state method

Within this method, we fit the two- and three-point functions keeping terms up to the first excited state, as detailed in Ref. [27]. Briefly, we use

$$C(\Gamma_0, \vec{q}, t_s) = c_0(\vec{q})e^{-E_N(\vec{q})t_s} + c_1(\vec{q})e^{-E^*(\vec{q})t_s}, \quad (17)$$

$$\begin{aligned} C^{\mu\nu}(\Gamma; \vec{q}; t_s, t_{\text{ins}}) &= A_{00}^{\mu\nu}(\Gamma, \vec{q})e^{-m_N(t_s - t_{\text{ins}}) - E_N(\vec{q})t_{\text{ins}}} \\ &+ A_{01}^{\mu\nu}(\Gamma, \vec{q})e^{-m_N(t_s - t_{\text{ins}}) - E^*(\vec{q})t_{\text{ins}}} \\ &+ A_{10}^{\mu\nu}(\Gamma, \vec{q})e^{-m_N^*(t_s - t_{\text{ins}}) - E_N(\vec{q})t_{\text{ins}}} \\ &+ A_{11}^{\mu\nu}(\Gamma, \vec{q})e^{-m_N^*(t_s - t_{\text{ins}}) - E^*(\vec{q})t_{\text{ins}}}, \end{aligned} \quad (18)$$

where  $m_N$  ( $m_N^*$ ) and  $E_N(\vec{q})$  ( $E^*(\vec{q})$ ) are the mass and energy of the ground (first excited) state with momentum  $\vec{q}$ , respectively. The ground state corresponds to a single particle, so its energy at finite momentum is given by the continuum dispersion relation,  $E_N(\vec{q}) = \sqrt{\vec{q}^2 + m_N^2}$ , where  $\vec{q} = \frac{2\pi}{L}\vec{n}$  with  $\vec{n}$  a lattice vector with components  $n_i \in (-\frac{L}{2a}, \frac{L}{2a}]$ . By modeling the ground and first excited state explicitly, the leading correction to the two-state fit method is expected to be due to the second excited state energy.

### 3. Summation method

Summing over  $t_{\text{ins}}$  in the ratio of Eq. (14) yields a geometric sum [28,29] from which we obtain

$$\begin{aligned} S^{\mu\nu}(\Gamma; \vec{q}; t_s) &= \sum_{t_{\text{ins}}=2a}^{t_s-2a} R^{\mu\nu}(\Gamma; \vec{q}; t_s, t_{\text{ins}}) \\ &= c + \Pi^{\mu\nu}(\Gamma; \vec{q})t_s + \mathcal{O}(e^{-m_N^*t_s}), \end{aligned} \quad (19)$$

where the ground state contribution,  $\Pi^{\mu\nu}(\Gamma; \vec{q})$ , is extracted from the slope of a linear fit with respect to  $t_s$ . The advantage of the summation method compared with the plateau method is that, despite the fact that it still assumes a single state dominance, the excited states are suppressed exponentially with respect to  $t_s$  instead of  $t_s - t_{\text{ins}}$ .

For all three methods, we carry out correlated fits to the data, i.e., we compute the covariance matrix  $C_{ij}$  between jackknife samples.

We illustrate our analysis in Fig. 1 by considering the extraction of  $g_T^{\mu-d}$  for the ensemble cC211.060.80 (see Table I). As can be seen, from the first and second columns, for  $g_T^{\mu-d}$  there are large excited state contributions that would require  $t_s > 2$  fm to suppress in the ratio [30]. Including the first excited state yields results that are consistent while varying  $t_s^{\text{low}}$ , which indicate that contributions from the second excited state are suppressed. Note that the approximately constant two-state fit errors as we increase  $t_s^{\text{low}}$  are due to the fact that we have higher statistics at large values of  $t_s$ , such that statistical errors in the ratio are approximately

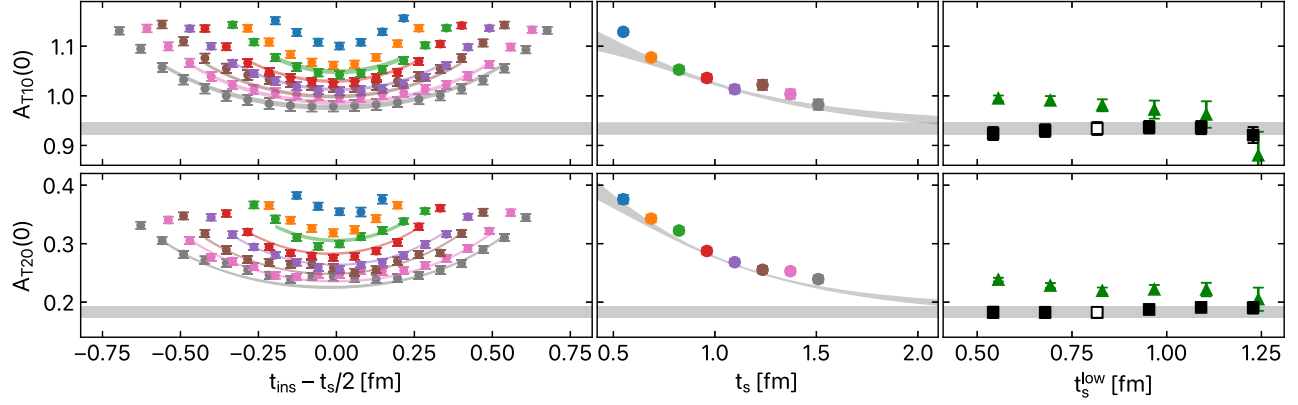


FIG. 1. We show the analysis of the ratio from which we extract  $g_T^{u-d} \equiv A_{T10}(0)$  (upper) and  $\langle x \rangle_{\delta u-\delta d} \equiv A_{T20}(0)$  (lower) for the cC211.060.80 ensemble. The left panels show the ratio versus the insertion time  $t_{\text{ins}}$  shifted by half the sink-source time  $t_s/2$ . The middle panels show the value of the central point of the ratio of Eq. (14), i.e., for  $t_{\text{ins}} = t_s/2$ . In the right panel, we show the values obtained when we perform a two-state fit (black squares) and the summation method (green triangles), as we vary the lower fit range,  $t_s^{\text{low}}$  used in the fits. The open symbol and horizontal gray band spanning the three panels show the value we take. The gray curved band in the middle panels shows the two-state fit prediction for the ratio for  $t_{\text{ins}} = t_s/2$  using the parameters determined by the open symbols.

constant with increasing  $t_s$ . The summation method, on the other hand, shows slower convergence as compared with the two-state fit, which indicates contributions from the first excited state are not sufficiently suppressed at the smaller values of  $t_s^{\text{low}}$  considered. A similar analysis is performed for the second Mellin GFFs. As an example, we show  $\langle x \rangle_{\delta u-\delta d}$  for ensemble cC211.060.80 in the lower panel of Fig. 1. As can be seen, the ratio also shows sizeable excited-state contamination. Including the first excited state in a two-state fit leads to a ground state matrix element that is significantly lower compared with the plateau method. For increasing  $t_s^{\text{low}}$  the summation fit agrees with the two-state fit. The latter yields consistent results for all  $t_s^{\text{low}}$ . Given the stability observed when using the two-state fit for varying  $t_s^{\text{low}}$ , we take this result as the best determination of the ground state matrix element. This is done throughout our analysis of the GFFs.

Unlike forward matrix elements, in general, the nucleon matrix elements of the operators in Eqs. (6) and (7) yield linear combinations of the GFFs in the nonforward limit depending on the insertion operator quantum numbers, the nucleon spin projection, and components of the momentum transfer. As mentioned previously, the expressions for the linear combinations of  $\Pi^{\mu\nu}(\Gamma; \vec{p})$ , for the different operators, are given in the Appendix. We construct an over-constrained system of equations that is inverted through a singular value decomposition to obtain the individual GFFs. For more details, see, e.g., Refs. [24,27,31].

The excited states' analysis for finite momentum transfer squared  $Q^2$  follows the same procedure as for  $Q^2 = 0$ . In Fig. 2 we show examples of the relevant ratios for the derivative operators for the case of the cC211.060.80 ensemble and for the first nonzero momentum, namely for  $Q^2 = 0.05 \text{ GeV}^2$ .

#### IV. RENORMALIZATION FUNCTIONS

The isovector operators considered here are multiplicatively renormalized. We obtain the renormalization functions (Z factors) nonperturbatively in the Rome-Southampton method (RI' scheme) [32], which is a mass-independent regularization. Thus, to appropriately take the chiral limit we use five ensembles of  $N_f = 4$  twisted mass quarks at different values of the pion mass. These ensembles are specifically generated for the renormalization program using the same  $\beta$  value as the three ensembles considered. For the calculation of the vertex functions we employ the momentum source method introduced in Ref. [33] and employed in Refs. [34–36] for twisted mass fermions. This method offers high statistical accuracy using a small number of gauge configurations. In the RI' scheme, the vertex momentum,  $p$ , is set equal to the renormalization scale  $\mu_0$

$$Z_{\mathcal{O}}(\mu_0) = \frac{Z_q(\mu_0)}{\frac{1}{12} \text{Tr}[\mathcal{V}_{\mathcal{O}}(p)(\Lambda_{\mathcal{O}}^{\text{tree}}(p))^{-1}]|_{p^2=\mu_0^2}}, \quad (20)$$

where  $\mathcal{V}_{\mathcal{O}}$  is the amputated vertex function of the operator under study. We define the renormalization functions for the quark field and quark operator as  $\psi^R = Z_q \psi^B$  and  $\mathcal{O}_T^R = Z_{\mathcal{O}} \mathcal{O}_T^B$ , respectively.  $Z_q$  is given by matching the propagator to its tree level value  $\Lambda_q^{\text{tree}}(p)$

$$Z_q(\mu_0) = \frac{1}{12} \text{Tr}[S^{-1}(p)\Lambda_q^{\text{tree}}(p)]|_{p^2=\mu_0^2}. \quad (21)$$

We extract  $Z_{\mathcal{O}}$  at several values of the renormalization scale, and each estimate is improved by subtracting finite lattice artifacts [37], which are calculated in perturbation theory. The chirally extrapolated values are then converted

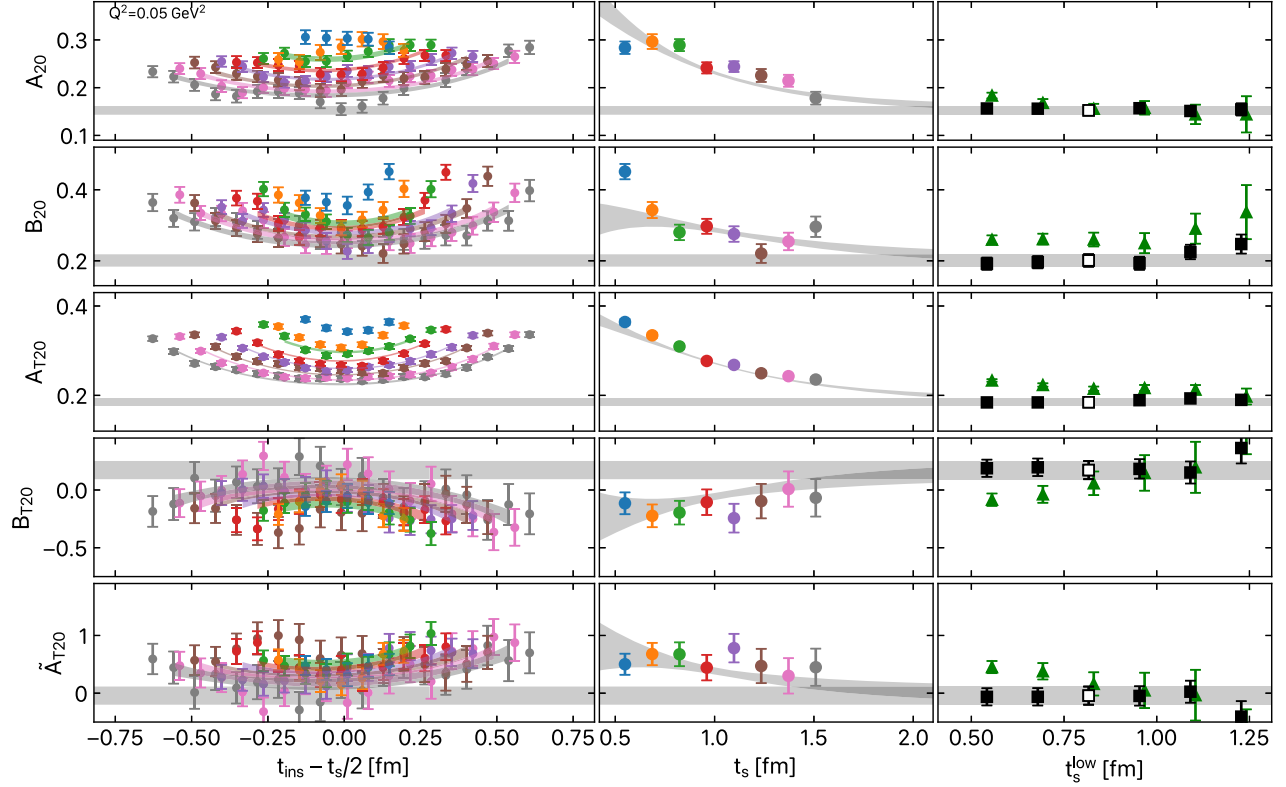


FIG. 2. The same analysis as Fig. 1 but for the two GFFs of the vector derivative operator,  $A_{20}$  and  $B_{20}$ , and the three GFFs of the tensor derivative operator  $A_{T20}$ ,  $B_{T20}$ , and  $\tilde{A}_{T20}$  for the first nonzero momentum transfer  $Q^2 = 0.05 \text{ GeV}^2$  of the cC211.060.80 ensemble.

to the  $\overline{\text{MS}}$  scheme at a scale of 2 GeV. For details on our approach, see Refs. [34–36]. In Table IV we provide the  $\overline{\text{MS}}$  estimates for the local and one-derivative tensor operators. Also, in Fig. 3 we show  $Z_T$  in the  $\overline{\text{MS}}$  scheme as a function of the initial RI' scale. We plot the purely nonperturbative estimates, as well as the improved ones, obtained by subtracting lattice artifacts computed in perturbation theory.

## V. RESULTS

### A. Fits of the $Q^2$ -dependence of GFFs

To fit the  $Q^2$ -dependence of the GFFs we use the  $p$ -pole ansatz [14,38],

$$F(Q^2) = \frac{F(0)}{(1 + Q^2/m_p^2)^p}. \quad (22)$$

This generalization of the more commonly used dipole ansatz allows the Mellin moments of the quark densities to fall off faster than  $1/Q^2$  when  $Q^2 \rightarrow \infty$ , as is expected from an explicit evaluation of the spinor products that relate the densities to the matrix elements [39]. Furthermore, the Fourier transform to impact parameter space, needed to obtain the moments of the transverse densities, can be carried out analytically for general  $p$ , as can the derivatives required in Eq. (1), yielding the modified Bessel functions. For more details on the motivation for using the  $p$ -pole ansatz and the expected values of  $p$  for each GFF, we refer to Ref. [14].

TABLE IV. Renormalization functions for the local tensor operator and one-derivative vector and tensor operators used in this work. The results are given in the  $\overline{\text{MS}}$  scheme at an energy scale of 2 GeV. The number in the first parentheses is the statistical error, while the number in the second parentheses corresponds to the systematic error obtained by varying the fit range in the  $(a\mu_0)^2 \rightarrow 0$  extrapolation or the systematic error coming from truncation effects in the perturbative conversion factors.

$\beta$	$Z_T$	$Z_{DV}^{\mu=\nu}$	$Z_{DV}^{\mu\neq\nu}$	$Z_{DT}^{\mu=\nu=\rho}$	$Z_{DT}^{\mu\neq\nu\neq\rho\neq\mu}$	$Z_{DT}^{\mu=\nu\neq\rho}$
1.778	0.847(1)(1)	1.151(1)(4)	1.160(1)(3)	1.182(1)(2)	1.198(1)(5)	1.154(1)(9)
1.836	0.863(1)(2)	1.137(1)(11)	1.169(1)(11)	1.215(1)(13)	1.240(1)(14)	1.171(1)(7)
1.900	0.887(1)(2)	1.173(1)(11)	1.195(1)(12)	1.257(1)(14)	1.277(1)(14)	1.198(1)(7)

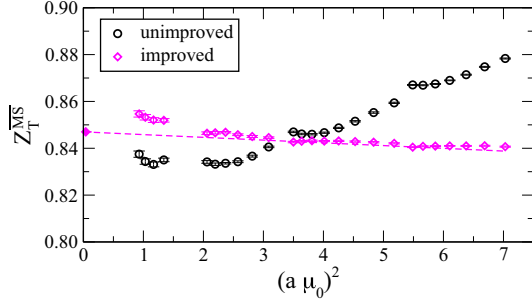


FIG. 3. The renormalization function  $Z_T$  for the local tensor operator at  $\beta = 1.778$ . The unimproved (improved) estimates are shown with black (magenta) points. The dashed line is the extrapolation to  $(a\mu_0)^2 \rightarrow 0$ , and the filled magenta point is the final estimate.

We perform a separate fit to each of the ten GFFs for each of the three ensembles. In general, there are three parameters in each fit, namely  $F(0)$ , the value of the GFF in the forward limit;  $m_p$ , the pole mass; and  $p$ , the exponent. Varying all three parameters leads to significant instabilities, as also observed in Refs. [40,41]. We therefore use Gaussian priors for  $p$  centered at  $p = 2$  with a width of 0.5. An exception is the case of  $A_{10}(Q^2)$ ,  $B_{10}(Q^2)$ ,  $A_{20}(Q^2)$ , and  $A_{T20}(Q^2)$ , for which we restrict to dipole fits, i.e., we fix  $p = 2$ . Furthermore, for the case of the Dirac form factor,  $A_{10}(Q^2)$ , we fix  $A_{10}(0) = 1$ , i.e., the proton charge.

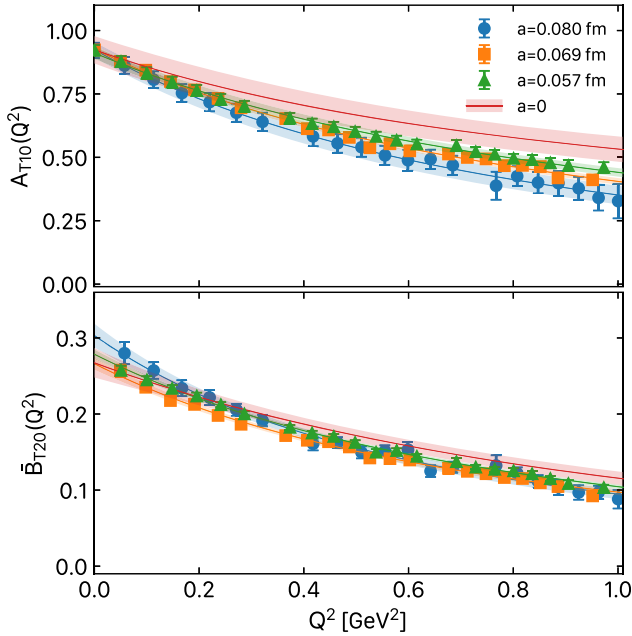


FIG. 4. The GFF  $A_{T10}$  (top) and  $\bar{B}_{T20}$  (bottom) for the cB211.072.64 (blue circles), cC211.060.80 (orange squares), and cD211.054.96 (green triangles) ensembles. Fits to the  $p$ -pole form of each ensemble are shown with the bands of same color. The continuum limit is also shown (red band), obtained as described in the text.

An example of the  $Q^2$  dependence of the GFFs is shown in Fig. 4 for the case of  $A_{T10}(Q^2)$  and  $\bar{B}_{T20}(Q^2)$ . Similar fits are carried out for all GFFs, yielding the five vector and five tensor GFFs for each ensemble.

## B. Continuum extrapolation

Our lattice formulation provides for automatic  $\mathcal{O}(a)$  improvement of all physical observables, and therefore we perform a linear fit in  $a^2$  to extrapolate the GFFs to  $a = 0$ .

In Fig. 5, we show the continuum limit of a selection of GFFs in the forward limit. As can be seen, for most of the cases the extrapolation is rather mild, and within the current statistical precision the extrapolation is well captured by a single term linear in  $a^2$  with a slope that in most cases is not very large.

In Table V, we quote the values of the GFFs shown in Fig. 5 at  $Q^2 = 0$  and in the continuum limit. Of particular interest is the continuum extrapolation of  $A_{T10}$  in the forward limit which yields the isovector tensor charge. This quantity plays a crucial role in the search for beyond the SM interactions [42] by experiments such as DUNE [43] and IsoDAR [44]. In Fig. 6, we compare our result,  $g_T^{u-d} = 0.924(54)$  [45], with those from other lattice QCD collaborations, all of which have used ensembles simulated with larger than physical pion mass thus requiring a chiral extrapolation to obtain their final value at the physical point. Phenomenological determinations of  $g_T$  are also compared in Fig. 6, obtained through the transversity (parton distribution function) PDF. The most recent result is obtained via a global analysis of electron-proton and proton-proton data yielding a value of  $g_T = 0.53(25)$  [6], somewhat lower and with larger uncertainty than lattice

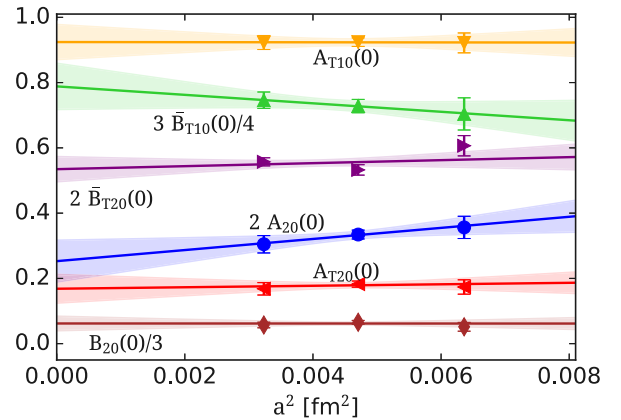


FIG. 5. Continuum limit of selected unpolarized and tensor GFFs in the forward limit as a function of  $a^2$ . The lines with their associated error bands are linear fits in  $a^2$ . Results for  $B_{20}(0)$ ,  $A_{20}(0)$ ,  $\bar{B}_{T20}(0)$ ,  $\bar{B}_{T10}(0)$ ,  $A_{T20}(0)$ , and  $A_{T10}(0)$  are presented with the name of each case being the closest to the corresponding band. We have scaled some of the quantities as indicated in the plot to avoid overlaps and improve presentation. Results are given in the  $\overline{\text{MS}}$  scheme at  $4 \text{ GeV}^2$ .

TABLE V. Our values of the forward limit of GFFs presented in Fig. 5 in the continuum limit.  $J^{u-d}$  is the isovector light quark contribution to the nucleon spin.

$g_T^{u-d} \equiv A_{T10}(0)$	$\kappa_T \equiv \bar{B}_{T10}(0)$	$\langle x \rangle_{u-d} \equiv A_{20}(0)$	$B_{20}(0)$	$J^{u-d} = \frac{1}{2}[A_{20}(0) + B_{20}(0)]$	$\langle x \rangle_{\delta u-\delta d} \equiv A_{T20}(0)$	$\bar{B}_{T20}(0)$
0.924(54)	1.051(94)	0.126(32)	0.186(67)	0.156(46)	0.168(44)	0.267(19)

QCD determinations. Planned measurements aim to reduce the error of the phenomenological value and allow for better comparison with the predicted lattice QCD value.

Beyond  $g_T$ , another challenging quantity that is poorly known is the anomalous tensor magnetic moment  $\kappa_T \equiv \bar{B}_{T10}(0)$ . It is a fundamental quantity, perhaps more than  $E_T$  and  $\tilde{H}_T$  [14], in describing the deformation of the transverse polarized quark distribution in an unpolarized nucleon. First lattice results were presented in the pioneering work of the QCDSF/UKQCD collaboration [40], where a value  $\kappa_T = 1.03(16)$  was reported obtained using chiral extrapolations from ensembles with pion masses of  $m_\pi > 400$  MeV. Our much improved analysis confirms their value using physical point ensembles and after taking the continuum limit. Having confirmed this value without the need of uncontrolled chiral extrapolations and at higher accuracy in the continuum limit, we can conclude that the phenomenological values  $\kappa_T = 0.81$  and  $1.24$  from two approaches using the constituent quark model [55] and  $\kappa_T = 1.73$  using the quark-soliton model [56] are incompatible and need to be revisited. Since  $\kappa_T \sim -h_1^+$  [57], our value confirms that the Boer-Mulders function,  $h_1^+$ , is negative and sizeable and corroborates the result found in a lattice QCD study of the transverse momentum dependent PDFs [58] computed using a mixed action scheme of domain wall valence fermions on staggered sea quarks with pion masses  $m_\pi = 369$  and  $518$  MeV.

The average momentum fraction,  $\langle x \rangle \equiv A_{20}(0)$ , is computed for the first time in the continuum limit without any chiral extrapolations. For the isovector momentum fraction,

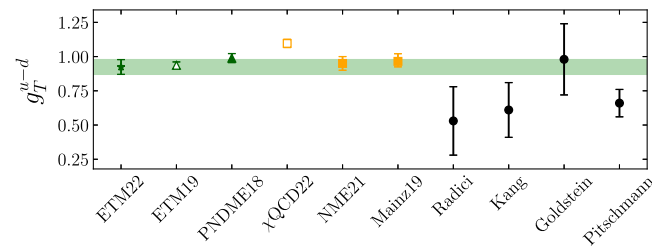


FIG. 6. We show lattice QCD results (green symbols for  $N_f = 2 + 1 + 1$  and yellow for  $N_f = 2 + 1$  ensembles) for  $g_T^{u-d}$  from ETMC [46,47] using only physical mass point ensembles; PNDME [48],  $\chi$ QCD [49], NME [50], and CLS-Mainz [51]. The PNDME and Mainz results are those cited as final results in the recent FLAG [52] report for  $N_f = 2 + 1 + 1$  and  $N_f = 2 + 1$ , respectively. Open green and yellow symbols denote lattice QCD results without continuum extrapolation. Results from phenomenology are shown with the black circles [5,6,53,54].

$\langle x \rangle_{u-d}$ , we find a value that is in agreement with the precise values extracted from phenomenology [59–61]. While the momentum fraction is well-known, this is not the case for  $B_{20}(0)$ , which is needed for the determination of the nucleon spin [62],  $J = [A_{20}(0) + B_{20}(0)]/2$ . With the isovector combinations of  $\langle x \rangle_{u-d}$  and our prediction for  $B_{20}(0)$ , we can compute the quark isovector contribution, i.e., the  $u - d$  contribution, to the spin of the nucleon ( $J^{u-d}$ ). From the values of  $A_{20}(0)$  and  $B_{20}(0)$  from Table V we find  $J^{u-d} = 0.156(46)$ . Note, however, that  $A_{20}(0)$  and  $B_{20}(0)$  exhibit dependence on the lattice spacing but with opposite slopes so that the resulting value of  $J^{u-d}$  in the continuum is compatible with our previous determination of  $J^{u-d} = 0.161(24)$  [2,27] obtained using only the cB211.072.64 ensemble.

For the second moment of the isovector transversity PDF  $\langle x \rangle_{\delta u-\delta d} \equiv A_{T20}(0)$ , as well as for  $\bar{B}_{T20}(0)$  there are no phenomenological results, and lattice QCD, thus, provides a prediction. We find a very mild dependence on the lattice spacing and, thus, a value in agreement with our previous study using the cB211.072.64 ensemble [27]. On the other hand and unlike the case for  $\kappa_T$ , QCDSF/UKQCD [40], using ensembles with pion masses  $m_\pi > 400$  MeV found a value of  $\bar{B}_{T20}(0) = 0.160(39)$ , which is lower than our value. This highlights the need to study these quantities with physical point ensembles. The RQCD collaboration [41], which included in their analysis one gauge ensemble with pion mass of  $160$  MeV, found a value compatible with ours.

For a review of lattice QCD results for  $g_T^{u-d}$ , we refer the reader to the 2021 FLAG review [52]. In addition to  $g_T^{u-d}$ , lattice QCD results for  $\langle x \rangle_{u-d}$  and  $\langle x \rangle_{\delta u-\delta d}$  are summarized in a recent community white paper, Ref. [63], and in the review of Ref. [64]. These reviews include our result obtained on the cB211.072.64 ensemble and from other collaborations which include ensembles at heavier than physical pion masses. As mentioned, the present work is the first to extract these quantities with three values of  $a$  at the physical point, thus eliminating the need for a chiral extrapolation.

After fitting the  $Q^2$  dependence of GFFs for each ensemble to the  $p$ -pole form as described above, the GFFs are available at any value of  $Q^2$ . We perform a linear fit in  $a^2$  at each of  $50$  common  $Q^2$  values, extrapolating to  $a = 0$ . While the ensembles at different values of  $a$  are independent, the GFFs evaluated at the  $50$   $Q^2$  values are correlated within the same ensemble, and this correlation is propagated to the continuum GFF by performing the linear extrapolation within a superjacker [65]. The resulting

GFFs in the continuum limit are shown in Fig. 7. As can be seen, the GFFs are determined with good precision, especially for the  $n = 1$  case. As expected, for the higher moment,  $n = 2$ , the GFFs have smaller values as compared with the  $n = 1$  GFFs. In addition, we observe that  $A_{20}(Q^2)$  and  $A_{T20}(Q^2)$  have a rather flat behavior.

Having the ten GFFs for 50 values of  $Q^2$  in the continuum limit, we perform fits to the  $p$ -pole form. We obtain the continuum fits for the ten GFFs shown in Fig. 7. The parameters of the fits to the  $Q^2$  dependence in the continuum are given in Table VI. The error in the parameters is estimated via superjackknife, obtained using the superjackknife samples from the  $a = 0$  extrapolation described above. Having determined the continuum form of the GFFs we can compute the first two moments of the transverse quark spin densities given in Eq. (1).

The Fourier transform to impact parameter space for a  $p$ -pole form is known [14] and given by

$$F(b_\perp^2) = \frac{m_p^2 F(0)}{2^p \pi \Gamma(p)} (m_p b_\perp)^{p-1} K_{p-1}(m_p b_\perp), \quad (23)$$

where  $\Gamma(x)$  is the Euler gamma function,  $K_n(x) = K_{-n}(x)$  the modified Bessel functions, and  $b_\perp = \sqrt{b_\perp^2}$ .  $F(b_\perp^2)$  is obtained for each GFF using the parameters in Table VI. The first and second moment of the probability density  $\rho(x, \vec{b}_\perp, \vec{s}_\perp, \vec{S}_\perp)$  are then constructed via Eq. (1) for four

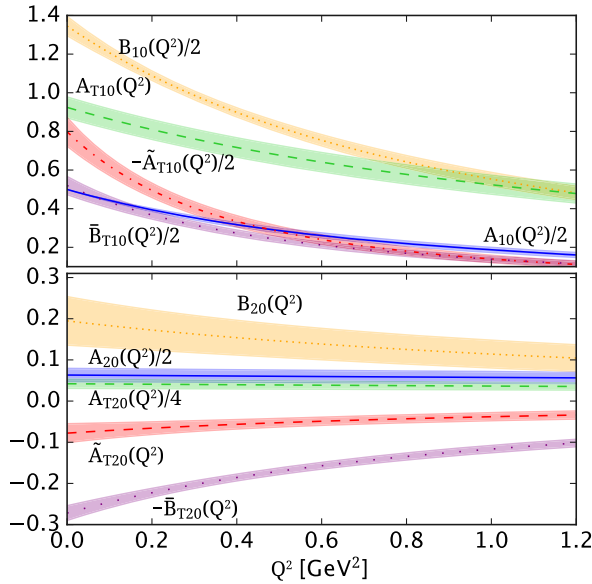


FIG. 7. Results for GFFs for  $n = 1$  (top) and  $n = 2$  (bottom) in the continuum limit as a function of the momentum transfer squared ( $Q^2$ ). Results for  $A_{n0}$ ,  $B_{n0}$ ,  $A_{Tn0}$ ,  $\tilde{A}_{Tn0}$ , and  $\tilde{B}_{Tn0}$  are presented with the name of each case being the closest to the corresponding band. We scale some GFFs as indicated in the plot to avoid overlaps and improve presentation. Results are given in the  $\overline{\text{MS}}$  at 2 GeV.

TABLE VI. The parameters obtained from fitting the  $Q^2$  dependence to the  $p$ -pole form after taking the continuum limit of the GFFs. Errors are obtained via a superjackknife analysis over the three ensembles used. Parameters with no errors were fixed for the corresponding fit.

GFF	$F(0)$	$m_p$ [GeV]	$p$
$A_{10}$	1	1.253(56)	2
$B_{10}$	2.691(99)	1.337(82)	2
$A_{T10}$	0.924(54)	1.45(19)	1.45(35)
$\tilde{B}_{T10}$	1.039(93)	1.01(11)	1.93(28)
$\tilde{A}_{T10}$	-1.60(15)	0.90(12)	2.16(34)
$A_{20}$	0.126(32)	4.52(46)	2
$B_{20}$	0.195(59)	1.61(27)	1.63(26)
$A_{T20}$	0.168(44)	3.66(51)	2
$\tilde{B}_{T20}$	0.272(18)	1.39(10)	2.04(10)
$\tilde{A}_{T20}$	0.427(54)	1.38(17)	1.872(70)

combinations of the transverse quark spin ( $\vec{s}_\perp$ ) and the transverse spin of the nucleon ( $\vec{S}_\perp$ ).

The first moment of the probability density,  $\langle 1 \rangle_\rho(x, \vec{b}_\perp, \vec{s}_\perp, \vec{S}_\perp)$  is shown in Fig. 8. It is very interesting that for all cases we observe a sizeable deformation. We consider four cases: (i) For unpolarized quarks in a transversely polarized nucleon, we observe a large distortion toward the positive  $b_y$  direction. This can be traced back to the GFF  $B_{10}$ , contributing to the term for  $E'$  of Eq. (1) that, as seen in Fig. 7, is large and decreases fast yielding a large derivative. The origin of this behavior is related to the Sivers effect [66], a connection that was made in Ref. [67]. (ii) For transversely polarized quarks in an unpolarized nucleon, we can also observe a distortion; however, it is much milder compared with the previous case. This is because in the isovector combination the  $\tilde{B}_{T10}(b_\perp^2)$  term contributing here has a milder  $Q^2$  dependence. This behavior is in contrast to that of the stronger  $Q^2$  dependence of the individual quark contributions to  $\tilde{B}_{T10}(b_\perp^2)$  observed in Ref. [40]. (iii) Another interesting case is when both quarks and the nucleon are transversely polarized. In this situation, all the terms in Eq. (1) contribute leading to a significant deformation of the density. (iv) If one chooses the polarization to be perpendicular between the quarks and the nucleon, the third term of Eq. (1) drops out, and the fourth one creates a significant impact, leading to a distortion also in the  $b_x$  direction.

In Fig. 9, we show the second moment of the probability densities,  $\langle x \rangle_\rho(x, \vec{b}_\perp, \vec{s}_\perp, \vec{S}_\perp)$ , for the same four cases discussed in Fig. 8. A general observation is that the distortion is milder and the densities are more localized around  $\vec{b}_\perp = \vec{0}$ . One reason is that  $A_{20}(Q^2)$  is relatively flat compared with  $A_{10}(Q^2)$ , leading to a rather localized density.

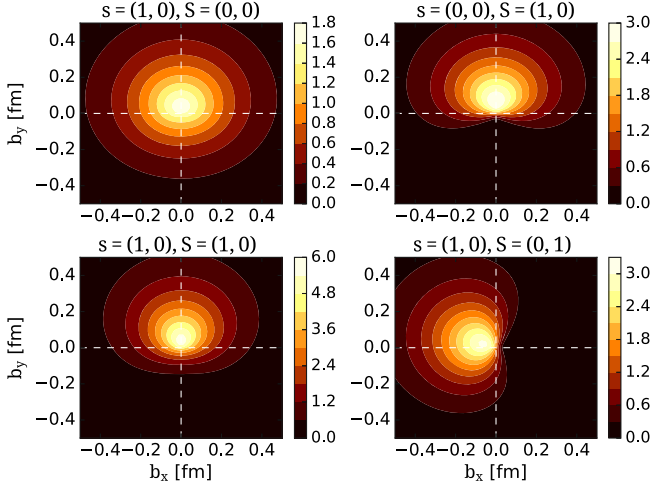


FIG. 8. Contours of the first moment of the probability density defined in Eq. (1),  $\langle 1 \rangle_\rho$  [ $\text{fm}^{-2}$ ] as a function of the two components of  $\vec{b}_\perp$ ,  $b_x$ , and  $b_y$ . Top left: transversely polarized quarks in an unpolarized nucleon. Top right: Unpolarized quarks in a transversely polarized nucleon. Bottom left: transversely polarized quarks in a transversely polarized nucleon. Bottom-right: same as the bottom-left but with perpendicular polarizations between them.

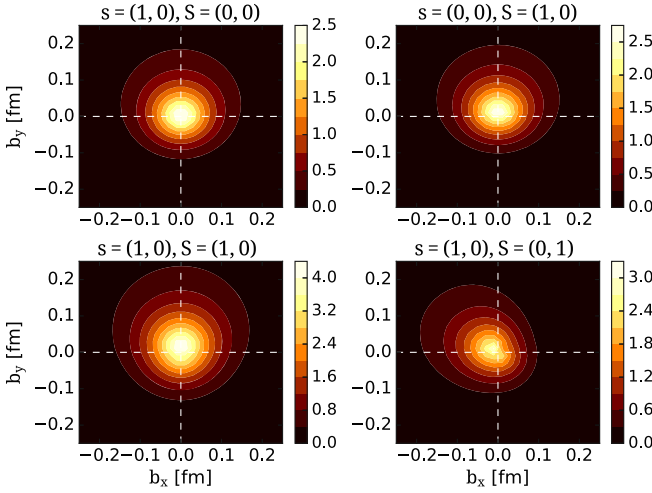


FIG. 9. Second moment of the probability density defined in Eq. (1)  $\langle x^2 \rangle_\rho$  [ $\text{fm}^{-2}$ ]. The notation is the same as in Fig. 8.

## VI. CONCLUSIONS

We present the first lattice QCD calculation of the first two Mellin moments of the isovector transverse quark spin densities in the nucleon in the continuum limit directly at the physical point. The calculation is performed using three twisted-mass fermion gauge ensembles with lattice spacings  $a \simeq 0.057, 0.069, 0.080$  fm enabling for the first time a controlled continuum extrapolation directly at the physical point avoiding uncontrolled errors due to the chiral extrapolation. We confirm the existence of a sizeable Sivvers and Boer-Mulders effect determining the

anomalous tensor magnetic moment  $\kappa_T = 1.051(94)$ . The results for the transverse quark spin densities demonstrate that significant deformations exist in the nucleon that are more prominent for the first moment. For the second moment the densities are more localized around the center of momentum of the proton.

## ACKNOWLEDGMENTS

We would like to thank all members of the Extended Twisted Mass Collaboration (ETMC) for a very constructive and enjoyable collaboration. M.C. acknowledges financial support by the U.S. Department of Energy Early Career Award under Grant No. DE-SC0020405. K.H. is financially supported by the project POST-DOC/0718/0100 and CULTURE-AWARD-YR/0220/0012 cofinanced by the European Regional Development Fund and the Republic of Cyprus through the Research and Innovation Foundation. S.B., J.F., and K.H. are financially supported by the EuroCC project (GA No. 951732) funded by the Deputy Ministry of Research, Innovation and Digital Policy and the Cyprus Research and Innovation Foundation and the European High-Performance Computing Joint Undertaking (JU) under Grant Agreement No. 951732. S.B. and J.F. are financially supported by the H2020 project PRACE 6-IP (GA No. 82376). The project acknowledges support from the European Joint Doctorate projects HPC-LEAP and STIMULATE funded by the European Union's Horizon 2020 research and innovation program under Grant Agreements No. 642069 and No. 765048, respectively. G.S. acknowledges financial support from H2020 project PRACE-6IP (Grant Agreement ID No. 823767). P.D. acknowledges support from the European Union's Horizon 2020 research and innovation program under the Marie Skłodowska-Curie Grant Agreement No. 813942 (EuroPLEX) and from INFN under the research project INFN-QCDLAT. Results were obtained using Piz Daint at Centro Svizzero di Calcolo Scientifico (CSCS), via the Project IDs No. s702, No. s954, and No. pr79. We thank the staff of CSCS for access to the computational resources and for their constant support. The authors gratefully acknowledge the Gauss Centre for Supercomputing e.V. ([www.gauss-centre.eu](http://www.gauss-centre.eu)) for funding this project by providing computing time on the GCS Supercomputer JUWELS at Jülich Supercomputing Centre (JSC) through the projects FSSH, PR74YO and CECY00, CHCH02 [John von Neumann Institute for Computing (NIC)]. Part of the results have been produced within the EA program of JUWELS Booster also with the help of the JUWELS Booster Project Team (JSC, Atos, ParTec, NVIDIA). We acknowledge the CINECA award under the ISCRA initiative, for the availability of high performance computing resources and support. We acknowledge PRACE for awarding us access to Marconi100 at CINECA (Italy), Piz-Daint at CSCS (Switzerland), and Hawk at

HLRS (Germany). We acknowledge the Gauss Centre for Supercomputing e.V. ([www.gauss-centre.eu](http://www.gauss-centre.eu)) for project pr74yo by providing computing time on SuperMUC at LRZ ([www.lrz.de](http://www.lrz.de)) and Juwels Booster at JSC. The authors acknowledge the Texas Advanced Computing Center (TACC) at The University of Texas at Austin for providing HPC resources (Project ID No. PHY21001).

### APPENDIX: PARAMETRIZATION OF MATRIX ELEMENTS

We present the decomposition of the nuclear matrix elements of the operators of interest employing different projectors in terms of Lorentz-invariant GFFs. The expressions are given in Euclidean space. We focus on the rest frame for the final state,  $p' = iE' = im$  and  $\vec{p} = -\vec{Q}$ , which is what is used in this work. For simplicity in the presentation we use  $m \equiv m_N$ . The normalization of the states is given by  $C = \sqrt{2m^2/E(E+m)}$ .

The local vector operator decomposes into the Dirac and Pauli form factors,

$$\begin{aligned} &\langle N(p', s') | \mathcal{O}_V^\mu | N(p, s) \rangle \\ &= \bar{u}_N(p', s') \left[ \gamma_\mu F_1(Q^2) - \frac{i\sigma_{\mu\nu}\Delta^\nu}{2m} F_2(Q^2) \right] u_N(p, s), \end{aligned} \quad (\text{A1})$$

where  $u_N(p, s)$  is the nucleon spinor. The parametrization for the ground state of the vector matrix elements,  $\Pi_V^\mu$ , projected with the unpolarized and polarized parity projectors, becomes

$$\Pi_V^\mu(\Gamma_0, \vec{p}) = C \frac{E+m}{2m} \left( F_1(Q^2) + \frac{Q^2}{4m^2} F_2(Q^2) \right), \quad (\text{A2})$$

$$\Pi_V^j(\Gamma_0, \vec{p}) = C \frac{p_j}{2m} \left( F_1(Q^2) + \frac{Q^2}{4m^2} F_2(Q^2) \right), \quad j \neq 0 \quad (\text{A3})$$

$$\Pi_V^j(\Gamma_k, \vec{p}) = C \frac{\epsilon_{j\rho k} p_\rho}{2m} (F_1(Q^2) + F_2(Q^2)), \quad j \neq 0, \quad (\text{A4})$$

where repeated indices are summed over.

The local tensor operator decomposes into three form factors, that is

$$\langle N(\vec{p}', s') | \mathcal{O}_T^{\mu\nu} | N(\vec{p}, s) \rangle = \bar{u}_N(\vec{p}', s') \left[ \sigma^{\mu\nu} A_{T10} + i \frac{\gamma^{[\mu} \Delta^{\nu]}}{2m} B_{T10} + \frac{\tilde{P}^{[\mu} \Delta^{\nu]}}{m^2} \tilde{A}_{T10} \right] u_N(p, s), \quad (\text{A5})$$

and, thus,

$$\Pi_T^{\mu\nu}(\Gamma_0; \vec{p}) = A_{T10} C \left( \frac{i(p_\mu \delta_{0\nu} - p_\nu \delta_{0\mu})}{2m} \right) + B_{T10} C \left( \frac{i(p_\mu \delta_{0\nu} - p_\nu \delta_{0\mu})}{2m} \right) + \tilde{A}_{T10} C \left( \frac{i(m+E)(p_\mu \delta_{0\nu} - p_\nu \delta_{0\mu})}{2m^2} \right), \quad (\text{A6})$$

$$\Pi_T^{\mu\nu}(\Gamma_k; \vec{p}) = A_{T10} C \left( \frac{im\epsilon_{\mu\nu k0} + p_\sigma \epsilon_{\mu\nu k\sigma}}{2m} \right) + B_{T10} C \left( \frac{(m(\delta_{0\mu} + \delta_{0\nu})\epsilon_{\mu\nu k\sigma} + i(p_\mu \epsilon_{\nu k0\sigma} - p_\nu \epsilon_{\mu k0\sigma}))p_\sigma}{4m^2} \right). \quad (\text{A7})$$

For the vector one-derivative operator we have three GFFs, given by

$$\langle N(p', s') | \mathcal{O}_V^{\mu\nu} | N(p, s) \rangle = \bar{u}_N(p', s') \left[ A_{20}(Q^2) \gamma^{\{\mu} \tilde{P}^{\nu\}} + B_{20}(Q^2) \frac{i\sigma^{\{\mu\alpha} Q_\alpha \tilde{P}^{\nu\}}}{2m} C_{20}(Q^2) \frac{q^{\{\mu} Q^{\nu\}}}{m} \right] u_N(p, s), \quad (\text{A8})$$

and we obtain

$$\Pi_V^{00}(\Gamma_0, \vec{p}) = A_{20} C \left( -\frac{3E}{8} - \frac{E^2}{4m} - \frac{m}{8} \right) + B_{20} C \left( -\frac{E}{8} + \frac{E^3}{8m^2} + \frac{E^2}{16m} - \frac{m}{16} \right) + C_{20} C \left( \frac{E}{2} - \frac{E^3}{2m^2} + \frac{E^2}{4m} - \frac{m}{4} \right), \quad (\text{A9})$$

$$\Pi_V^{jj}(\Gamma_0, \vec{p}) = A_{20} C \left( \frac{E}{8} + \frac{m}{8} + \frac{p_j^2}{4m} \right) + B_{20} C \left( -\frac{E^2}{16m} + \frac{m}{16} - \frac{p_j^2 E}{8m^2} + \frac{p_j^2}{8m} \right) + C_{20} C \left( -\frac{E^2}{4m} + \frac{m}{4} + \frac{p_j^2 E}{2m^2} + \frac{p_j^2}{2m} \right), \quad (\text{A10})$$

$$\Pi_V^{jj}(\Gamma_k, \vec{p}) = A_{20} C \left( -i \frac{\epsilon_{jk0\rho} p_j p_\rho}{4m} \right) + B_{20} C \left( -i \frac{\epsilon_{jk0\rho} p_j p_\rho}{4m} \right), \quad (\text{A11})$$

$$\Pi_V^{j0}(\Gamma_0, \vec{p}) = A_{20}C\left(i\frac{p_j}{4} + i\frac{p_j E}{4m}\right) + B_{20}C\left(i\frac{p_j}{8} - i\frac{p_j E^2}{8m^2}\right) + C_{20}C\left(-i\frac{p_j}{2} + i\frac{p_j E^2}{2m^2}\right), \quad (\text{A12})$$

$$\Pi_V^{j0}(\Gamma_k, \vec{p}) = A_{20}C\left(-\epsilon_{jk0\rho}\left(-\frac{p_\rho}{8} - \frac{p_\rho E}{8m}\right)\right) + B_{20}C\left(-\epsilon_{jk0\rho}\left(-\frac{p_\rho}{8} - \frac{p_\rho E}{8m}\right)\right) \quad (\text{A13})$$

$$\Pi_V^{jl}(\Gamma_0, \vec{p}) = A_{20}C\frac{p_j p_l}{4m} + B_{20}C\left(-\frac{p_j p_l E}{8m^2} + \frac{p_j p_l}{8m}\right) + C_{20}C\left(\frac{p_j p_l E}{2m^2} + \frac{p_j p_l}{2m}\right), \quad (\text{A14})$$

$$\Pi_V^{jl}(\Gamma_k, \vec{p}) = A_{20}C\left(-i\frac{\epsilon_{jk0\rho} p_l p_\rho}{8m} - i\frac{\epsilon_{lk0\rho} p_j p_\rho}{8m}\right) + B_{20}C\left(-i\frac{\epsilon_{jk0\rho} p_l p_\rho}{8m} - i\frac{\epsilon_{lk0\rho} p_j p_\rho}{8m}\right). \quad (\text{A15})$$

According to Refs. [15,39,68] the one-derivative tensor operator decomposes into four GFFs, namely  $A_{T20}$ ,  $B_{T20}$ ,  $\tilde{A}_{T20}$ , and  $\tilde{B}_{T21}$  as Eq. (11):

$$\langle N(p', s') | \mathcal{O}_T^{\mu\nu\rho} | N(p, s) \rangle = \bar{u}_N(p', s') \left[ i\sigma^{\mu\nu} \bar{P}^\rho A_{T20} + \frac{\gamma^{[\mu} \Delta^{\nu]}}{2m} \bar{P}^\rho B_{T20} + i\frac{\bar{P}^{[\mu} \Delta^{\nu]}}{m^2} \bar{P}^\rho \tilde{A}_{T20} + \frac{\gamma^{[\mu} \bar{P}^{\nu]}}{m} \Delta^\rho \tilde{B}_{T21} \right] u_N(p, s). \quad (\text{A16})$$

Depending on the projector  $\Gamma_0$  or  $\Gamma_k$  used we obtain

$$\begin{aligned} \Pi_T^{\mu\nu\rho}(\Gamma_0; \vec{p}) &= A_{T20}C\left(\frac{i((m+E)p_\mu \delta_{\nu\rho} - 6mp_\mu \delta_{0\nu\rho} - p_\nu((m+E)\delta_{\mu\rho} - 6m\delta_{0\mu\rho}))}{16m}\right. \\ &\quad \left. + \frac{\delta_{0\mu}(m(m+E)\delta_{\nu\rho} + 6p_\nu p_\rho) - \delta_{0\nu}(m(m+E)\delta_{\mu\rho} + 6p_\mu p_\rho)}{16m}\right) \\ &\quad + \tilde{A}_{T20}C\left(\frac{i(m+E)((m+E)p_\mu \delta_{\nu\rho} - 6mp_\mu \delta_{0\nu\rho} - p_\nu((m+E)\delta_{\mu\rho} - 6m\delta_{0\mu\rho}))}{16m^2}\right. \\ &\quad \left. - \frac{(m+E)(\delta_{0\nu}(m(m+E)\delta_{\mu\rho} + 6p_\mu p_\rho) - \delta_{0\mu}(m(m+E)\delta_{\nu\rho} + 6p_\nu p_\rho))}{16m^2}\right) \\ &\quad + B_{T20}C\left(\frac{i((m+E)p_\mu \delta_{\nu\rho} - 6mp_\mu \delta_{0\nu\rho} - p_\nu((m+E)\delta_{\mu\rho} - 6m\delta_{0\mu\rho}))}{16m}\right. \\ &\quad \left. + \frac{\delta_{0\mu}(m(m+E)\delta_{\nu\rho} + 6p_\nu p_\rho) - \delta_{0\nu}(m(m+E)\delta_{\mu\rho} + 6p_\mu p_\rho)}{16m}\right) \end{aligned} \quad (\text{A17})$$

$$\begin{aligned} \Pi_T^{\mu\nu\rho}(\Gamma_k; \vec{p}) &= iA_{T20}C\left(i\frac{(p_\sigma(2\delta_{0\rho}\epsilon_{\mu\nu k\sigma} + \delta_{0\nu}\epsilon_{\mu\rho k\sigma} - \delta_{0\mu}\epsilon_{\nu\rho k\sigma}) + p_\mu(-\epsilon_{\nu\rho k0}) + p_\nu\epsilon_{\mu\rho k0} + 2p_\rho\epsilon_{\mu\nu k0})}{8}\right. \\ &\quad \left. + \frac{p_\sigma(p_\mu(-\epsilon_{\nu\rho k\sigma}) + p_\nu\epsilon_{\mu\rho k\sigma} + 2p_\rho\epsilon_{\mu\nu k\sigma}) - m^2(\delta_{0\mu} + \delta_{0\nu} - 2\delta_{0\rho})\epsilon_{\mu\nu\rho k}}{8m}\right) \\ &\quad + iB_{T20}C\left(\frac{3ip_\sigma(m^2(\delta_{0\mu\rho} + \delta_{0\nu\rho})\epsilon_{\mu\nu k\sigma} + p_\rho(p_\mu\epsilon_{\nu k0\sigma} - p_\nu\epsilon_{\mu k0\sigma}))}{16m^2}\right. \\ &\quad \left. + \frac{p_\sigma(-2p_\mu\delta_{0\nu}\epsilon_{\nu\rho k\sigma} + p_\mu\delta_{0\rho}\epsilon_{\nu\rho k\sigma} + 2p_\nu\delta_{0\mu}\epsilon_{\mu\rho k\sigma} - p_\nu\delta_{0\rho}\epsilon_{\mu\rho k\sigma} + p_\rho(\delta_{0\mu} + \delta_{0\nu})\epsilon_{\mu\nu k\sigma})}{16m}\right) \\ &\quad + i\tilde{B}_{T21}C\left(\frac{3ip_\sigma(m^2(\delta_{0\mu\rho} + \delta_{0\nu\rho})\epsilon_{\mu\nu k\sigma} + p_\rho(p_\mu\epsilon_{\nu k0\sigma} - p_\nu\epsilon_{\mu k0\sigma}))}{8m^2}\right. \\ &\quad \left. - \frac{p_\sigma(-2p_\mu\delta_{0\nu}\epsilon_{\nu\rho k\sigma} + p_\mu\delta_{0\rho}\epsilon_{\nu\rho k\sigma} + 2p_\nu\delta_{0\mu}\epsilon_{\mu\rho k\sigma} - p_\nu\delta_{0\rho}\epsilon_{\mu\rho k\sigma} + p_\rho(\delta_{0\mu} + \delta_{0\nu})\epsilon_{\mu\nu k\sigma})}{8m}\right). \end{aligned} \quad (\text{A18})$$

- [1] X. Ji, F. Yuan, and Y. Zhao, *Nat. Rev. Phys.* **3**, 27 (2021).
- [2] C. Alexandrou, S. Bacchio, M. Constantinou, J. Finkenrath, K. Hadjiyiannakou, K. Jansen, G. Koutsou, H. Panagopoulos, and G. Spanoudes, *Phys. Rev. D* **101**, 094513 (2020).
- [3] G. Wang, Y.-B. Yang, J. Liang, T. Draper, and K.-F. Liu (chiQCD Collaboration), *Phys. Rev. D* **106**, 014512 (2022).
- [4] M. Radici, A. Courtoy, A. Bacchetta, and M. Guagnelli, *J. High Energy Phys.* **05** (2015) 123.
- [5] Z.-B. Kang, A. Prokudin, P. Sun, and F. Yuan, *Phys. Rev. D* **93**, 014009 (2016).
- [6] M. Radici and A. Bacchetta, *Phys. Rev. Lett.* **120**, 192001 (2018).
- [7] R. Abdul Khalek *et al.*, *Nucl. Phys.* **A1026**, 122447 (2022).
- [8] J. P. Chen, H. Gao, T. K. Hemmick, Z. E. Meziani, and P. A. Souder (SoLID) (2014).
- [9] Z. Zhao, T. Liu, and H. Gao, *Proc. Sci. SPIN2018* (**2019**) 175.
- [10] C. Alexandrou *et al.*, *Phys. Rev. D* **98**, 054518 (2018).
- [11] C. Alexandrou, *J. Phys. Soc. Jpn. Conf. Proc.* **37**, 011013 (2022).
- [12] C. Alexandrou, S. Bacchio, J. Finkenrath, A. Frommer, K. Kahl, and M. Rottmann, *Phys. Rev. D* **94**, 114509 (2016).
- [13] C. Alexandrou, S. Bacchio, and J. Finkenrath, *Comput. Phys. Commun.* **236**, 51 (2019).
- [14] M. Diehl and P. Hagler, *Eur. Phys. J. C* **44**, 87 (2005).
- [15] M. Diehl, *Phys. Rep.* **388**, 41 (2003).
- [16] R. Frezzotti and G. C. Rossi, *J. High Energy Phys.* **08** (2004) 007.
- [17] R. Frezzotti, P. A. Grassi, S. Sint, and P. Weisz (Alpha Collaboration), *J. High Energy Phys.* **08** (2001) 058.
- [18] M. Constantinou *et al.* (ETM Collaboration), *J. High Energy Phys.* **08** (2010) 068.
- [19] J. Finkenrath *et al.*, *Proc. Sci. LATTICE2021* (**2022**) 284 [arXiv:2201.02551].
- [20] C. Alexandrou *et al.* (Extended Twisted Mass Collaboration), *Phys. Rev. D* **104**, 074515 (2021).
- [21] C. Alexandrou, S. Gusken, F. Jegerlehner, K. Schilling, and R. Sommer, *Nucl. Phys.* **B414**, 815 (1994).
- [22] S. Gusken, *Nucl. Phys. B, Proc. Suppl.* **17**, 361 (1990).
- [23] M. Albanese *et al.* (APE Collaboration), *Phys. Lett. B* **192**, 163 (1987).
- [24] C. Alexandrou, M. Constantinou, S. Dinter, V. Drach, K. Jansen, C. Kallidonis, and G. Koutsou, *Phys. Rev. D* **88**, 014509 (2013).
- [25] C. Alexandrou, M. Brinet, J. Carbonell, M. Constantinou, P. A. Harraud, P. Guichon, K. Jansen, T. Korzec, and M. Papinutto, *Phys. Rev. D* **83**, 094502 (2011).
- [26] C. Alexandrou, G. Koutsou, J. W. Negele, and A. Tsapalis, *Phys. Rev. D* **74**, 034508 (2006).
- [27] C. Alexandrou *et al.*, *Phys. Rev. D* **101**, 034519 (2020).
- [28] L. Maiani, G. Martinelli, M. L. Paciello, and B. Taglienti, *Nucl. Phys.* **B293**, 420 (1987).
- [29] S. Capitani, M. Della Morte, G. von Hippel, B. Jager, A. Juttner, B. Knippschild, H. B. Meyer, and H. Wittig, *Phys. Rev. D* **86**, 074502 (2012).
- [30] O. Bär, *Phys. Rev. D* **94**, 054505 (2016).
- [31] C. Alexandrou, J. Carbonell, M. Constantinou, P. A. Harraud, P. Guichon, K. Jansen, C. Kallidonis, T. Korzec, and M. Papinutto, *Phys. Rev. D* **83**, 114513 (2011).
- [32] G. Martinelli, C. Pittori, C. T. Sachrajda, M. Testa, and A. Vladikas, *Nucl. Phys.* **B445**, 81 (1995).
- [33] M. Gockeler, R. Horsley, H. Oelrich, H. Perlt, D. Petters, P. E. L. Rakow, A. Schafer, G. Schierholz, and A. Schiller, *Nucl. Phys.* **B544**, 699 (1999).
- [34] C. Alexandrou, M. Constantinou, T. Korzec, H. Panagopoulos, and F. Stylianou, *Phys. Rev. D* **83**, 014503 (2011).
- [35] C. Alexandrou, M. Constantinou, T. Korzec, H. Panagopoulos, and F. Stylianou, *Phys. Rev. D* **86**, 014505 (2012).
- [36] C. Alexandrou, M. Constantinou, and H. Panagopoulos (ETM Collaboration), *Phys. Rev. D* **95**, 034505 (2017).
- [37] M. Constantinou, R. Horsley, H. Panagopoulos, H. Perlt, P. E. L. Rakow, G. Schierholz, A. Schiller, and J. M. Zanotti, *Phys. Rev. D* **91**, 014502 (2015).
- [38] D. Brömmel *et al.* (QCDSF/UKQCD Collaborations), *Eur. Phys. J. C* **51**, 335 (2007).
- [39] M. Diehl, *Eur. Phys. J. C* **19**, 485 (2001).
- [40] M. Göckeler, P. Hägler, R. Horsley, Y. Nakamura, D. Pleiter, P. E. L. Rakow, A. Schäfer, G. Schierholz, H. Stüben, and J. M. Zanotti (QCDSF, UKQCD Collaborations), *Phys. Rev. Lett.* **98**, 222001 (2007).
- [41] G. S. Bali, S. Collins, M. Göckeler, R. Rödl, A. Schäfer, and A. Sternbeck, *Phys. Rev. D* **100**, 014507 (2019).
- [42] A. Courtoy, S. Baeßler, M. González-Alonso, and S. Liuti, *Phys. Rev. Lett.* **115**, 162001 (2015).
- [43] I. Bischer and W. Rodejohann, *Phys. Rev. D* **99**, 036006 (2019).
- [44] M. Abs *et al.*, arXiv:1511.05130.
- [45] C. Alexandrou *et al.*, *Proc. Sci. LATTICE2022* (**2023**) 092 [arXiv:2210.05743].
- [46] C. Alexandrou *et al.*, arXiv:2202.09871.
- [47] C. Alexandrou, S. Bacchio, M. Constantinou, J. Finkenrath, K. Hadjiyiannakou, K. Jansen, G. Koutsou, and A. Vaquero Aviles-Casco, *Phys. Rev. D* **102**, 054517 (2020).
- [48] R. Gupta, Y.-C. Jang, B. Yoon, H.-W. Lin, V. Cirigliano, and T. Bhattacharya, *Phys. Rev. D* **98**, 034503 (2018).
- [49] D. Horkel, Y. Bi, M. Constantinou, T. Draper, J. Liang, K.-F. Liu, Z. Liu, and Y.-B. Yang ( $\chi$ QCD Collaboration), *Phys. Rev. D* **101**, 094501 (2020).
- [50] S. Park, R. Gupta, B. Yoon, S. Mondal, T. Bhattacharya, Y.-C. Jang, B. Joó, and F. Winter (Nucleon Matrix Elements (NME) Collaboration), *Phys. Rev. D* **105**, 054505 (2022).
- [51] T. Harris, G. von Hippel, P. Jannarkar, H. B. Meyer, K. Ottnad, J. Wilhelm, H. Wittig, and L. Wrang, *Phys. Rev. D* **100**, 034513 (2019).
- [52] Y. Aoki *et al.* (Flavour Lattice Averaging Group (FLAG)), *Eur. Phys. J. C* **82**, 869 (2022).
- [53] G. R. Goldstein, J. O. Gonzalez Hernandez, and S. Liuti, arXiv:1401.0438.
- [54] M. Pitschmann, C.-Y. Seng, C. D. Roberts, and S. M. Schmidt, *Phys. Rev. D* **91**, 074004 (2015).
- [55] B. Pasquini, M. Pincetti, and S. Boffi, *Phys. Rev. D* **72**, 094029 (2005).
- [56] T. Ledwig, A. Silva, and H.-C. Kim, *Phys. Rev. D* **82**, 054014 (2010).
- [57] M. Burkardt, *Phys. Rev. D* **72**, 094020 (2005).
- [58] B. U. Musch, P. Hagler, M. Engelhardt, J. W. Negele, and A. Schafer, *Phys. Rev. D* **85**, 094510 (2012).

- [59] R. D. Ball *et al.* (NNPDF Collaboration), *Eur. Phys. J. C* **77**, 663 (2017).
- [60] S. Dulat, T.-J. Hou, J. Gao, M. Guzzi, J. Huston, P. Nadolsky, J. Pumplin, C. Schmidt, D. Stump, and C. P. Yuan, *Phys. Rev. D* **93**, 033006 (2016).
- [61] L. A. Harland-Lang, A. D. Martin, P. Motylinski, and R. S. Thorne, *Eur. Phys. J. C* **75**, 204 (2015).
- [62] X.-D. Ji, *Phys. Rev. Lett.* **78**, 610 (1997).
- [63] H.-W. Lin *et al.*, *Prog. Part. Nucl. Phys.* **100**, 107 (2018).
- [64] M. Constantinou *et al.*, *Prog. Part. Nucl. Phys.* **121**, 103908 (2021).
- [65] J. D. Bratt *et al.* (LHPC Collaboration), *Phys. Rev. D* **82**, 094502 (2010).
- [66] M. Bury, A. Prokudin, and A. Vladimirov, *J. High Energy Phys.* **05** (2021) 151.
- [67] M. Burkardt, *Nucl. Phys.* **A735**, 185 (2004).
- [68] P. Hagler, *Phys. Lett. B* **594**, 164 (2004).